Seasonal and Interannual Variability of the Tropical Maritime Continent Upper-Ocean Carbon Cycle Over the Last Decade: Results from a Newly Developed Regional Scale Model

Faisal Amri[1], Takashi Nakamura[1], Atsushi Watanabe[2], Aditya R. Kartadikaria[3], and Kazuo Nadaoka[1]

[1]Tokyo Institute of Technology
[2]The Sasakawa Peace Foundation
[3]Bandung Institute of Technology

November 26, 2022

Abstract

A three-dimensional physical-biogeochemical ocean numerical model with eddy-permitting horizontal resolution was applied to simulate upper-ocean carbon cycle variabilities in the Tropical Maritime Continent (TMC) over the last decade (2010–2019). Forced by atmospheric and oceanic reanalysis products with high temporal resolution, the model showed robust consistency with the observed seasonality of pCO2 and atmospheric CO2 sink/source characteristics across the modeling domain. Within the TMC, the model results indicated strong CO2 degassing along the west of Sumatra-south of Java associated with the seasonal cycle of the upwelling system in the area. While acting as a full-year atmospheric CO2 source, the TMC exhibited pronounced interannual modulation in both pCO2 and sea-air CO2 flux over the last decade. Large-scale anomalous strong CO2 degassing from 2015 to 2016 in response to the evolution of the 2015/2016 El Niño was observed from the simulation results. Modulations related to the Indian Ocean Dipole (IOD), on the other hand, were confined along the west of Sumatra-south of Java with a higher magnitude compared with anomalies related to El Niño/La Niña. Simulation results also captured the asymmetric response of the upper-ocean carbon cycle to the IOD over the last decade, where anomalies during negative IOD (nIOD) were notably strong despite being indicated as weak nIOD events by the Dipole Mode Index.

Seasonal and Interannual Variability of the Tropical Maritime Continent Upper-Ocean Carbon Cycle Over the Last Decade: Results from a Newly Developed Regional Scale Model

Faisal Amri[1], Takashi Nakamura[1], Atsushi Watanabe[2], A.R. Kartadikaria[3], and Kazuo Nadaoka[1]

[1]Transdisciplinary Science and Engineering Department, Tokyo Institute of Technology, Tokyo, Japan

[2]Ocean Policy Research Institute, The Sasakawa Peace Foundation, Japan

[3] Faculty of Earth Sciences and Technology, Oceanography Research Group, Institut Teknologi Bandung, Bandung, Indonesia

Corresponding author: Faisal Amri (amri.f.aa@m.titech.ac.jp/faisal.amri.os12@gmail.com)

Key Points:

- The Tropical Maritime Continent Sea surface acted as a full-year atmospheric CO_2 source with average flux of 0.08 PgC per year
- Strong pCO_2 and CO_2 degassing during Boreal Summer-Boreal Autumn around the West of Sumatra-South of Java was related to upwelling cycle
- Large-scale stronger-than-usual CO_2 degassing from Tropical Maritime Continent Sea surface during the development of the 2015/2016 El Niño

Abstract

A three-dimensional physical-biogeochemical ocean numerical model with eddy-permitting horizontal resolution was applied to simulate upper-ocean carbon cycle variabilities in the Tropical Maritime Continent (TMC) over the last decade (2010–2019). Forced by atmospheric and oceanic reanalysis products with high temporal resolution, the model showed robust consistency with the observed seasonality of pCO_2 and atmospheric CO_2 sink/source characteristics across the modeling domain. Within the TMC, the model results indicated strong CO_2 degassing along the west of Sumatra-south of Java associated with the seasonal cycle of the upwelling system in the area. While acting as a full-year atmospheric CO_2 source, the TMC exhibited pronounced interannual modulation in both pCO_2 and sea-air CO_2 flux over the last decade. Large-scale anomalous strong CO_2 degassing from 2015 to 2016 in response to the evolution of the 2015/2016 El Niño was observed from the simulation results. Modulations related to the Indian Ocean Dipole (IOD), on the other hand, were confined along the west of Sumatra-south of Java with a higher magnitude compared with anomalies related to El Niño/La Niña. Simulation results also captured the asymmetric response of the upper-ocean carbon cycle to the IOD over the last decade, where anomalies during negative IOD (nIOD) were notably strong despite being indicated as weak nIOD events by the Dipole Mode Index.

Plain Language Summary

The lack of long-term observational data has limited research on sea-air CO_2 exchange variabilities in the Tropical Maritime Continent (TMC). In this study, we provide results of the initial effort in modeling sea-air CO_2 exchange across the region over the last decade (2010-2019). The simulation results suggest that while the sea surface across the area acts as a CO_2 source to the atmosphere,

some periods like 2015-2016 were associated with stronger-than-usual degassing. Such anomalies are related to large-scale changes in the Pacific and Indian oceans.

1 Introduction

The Tropical Maritime Continent (TMC) region acts as a water passage that allows Pacific Ocean water to be transported to the Indian Ocean as part of thermohaline circulation, which modulates the global climate system (Gordon, 1986; Wyrtki, 1961). Located between the Indian and Pacific Ocean, the TMC area is subject to modulation caused by variabilities occurring in these two ocean basins, including the El Niño-Southern Oscillation (ENSO) in the tropical Pacific Ocean, and Indian Ocean Dipole (IOD) in the Indian Ocean (Ashok et al., 2003; Saji and Yamagata, 2003; Sprintall et al., 2014). Recent studies have confirmed that these climate modes influence the TMC area through sea-air interaction perturbation, which affects the rainfall rate and oceanic properties such as sea surface temperature, sea surface height, and circulation pattern (Delman et al., 2016; Pujiana et al., 2019, 2020; Saji and Yamagata, 2003; Siswanto et al., 2020; Sprintall et al., 2014; Susanto et al., 2001; Syamsudin et al., 2004).

Despite the progress, studies on oceanic carbon cycle dynamics in the area remain very limited compared to the number of oceanic carbon-related studies that are growing globally (Bakker et al., 2016; Key et al., 2004; Takahashi et al., 2002, 2009). Although one of the latest observation-based studies by Kartadikaria et al. (2015) on the compilation of sea surface CO_2 partial pressure (pCO_2) across the Indonesian seas could provide a general view of the atmospheric CO_2 sink/source characteristics, it still could not represent the actual seasonal cycle and response of the seawater CO_2 system to large-scale climate variabilities. Typical pCO_2 underway measurements conducted in a short period are not reliable in capturing the low-frequency variabilities that usually develop within an interannual time scale or longer (Sutton et al., 2017b). A study by Hamzah et al. (2020)

in western Indonesian seas later confirmed this issue by highlighting the possible variation in the carbonate system over seasonal and interannual timescales in the undersampled area. The recent development of the pCO_2 empirical model (Iida et al., 2015) or machine learning in estimating pCO_2 is unfortunately still inadequate and produces a relatively coarse resolution for resolving the complex island configuration within the TMC. These constraints make it challenging to apprehend TMC oceanic carbon cycle variabilities at various time scales.

Several modeling studies have indicated that the pCO_2 and sea-air CO_2 flux exhibit apparent modulation related to climate variability. A modeling study by Chai et al. (2009) in the South China Sea showed that pCO_2 followed the seasonal variations of net primary productivity, which was inversely correlated with the sea surface temperature (SST) anomaly in the Eastern Tropical Pacific region (NINO 3). Global scale modeling by Obata and Kitamura (2003) emphasized the Tropical Pacific Ocean region's sea-air CO_2 flux, where the variability in the region related to ENSO contributed approximately 70% to the global variability. Similar global-scale modeling was conducted by Valsala et al. (2014); despite indicating differences in the contribution of Tropical Pacific CO_2 flux variabilities to global variabilities, the study still agrees to the extent that Tropical Pacific Ocean variability has a significant influence on global carbon cycle modulation. They further suggested a stronger influence of El Niño-Modoki (Ashok et al., 2007) on carbon cycle variability in the western part of the Tropical Pacific, adjacent to the TMC. In their modeling study, Xiu and Chai (2014) also addressed the significance of the Pacific Decadal Oscillation and North Pacific Gyre Oscillation in modulating the sea-air CO_2 flux across the North Pacific region, highlighting the variabilities in much lower frequency domains. These studies partly confirm the hypothesis about the possible low-frequency modulation of the oceanic carbon cycle, considering the proximity of the TMC to the area studied previously. One of the remaining questions concerns

the modulation pattern related to the Indo-Pacific climate variability in the area, which this study attempts to address.

A newly developed low-trophic ecosystem model was employed to further resolve the issue of elucidating the upper-ocean carbon cycle variability across the TMC. The model was forced by realistic high-temporal resolution atmospheric forcings to approach the actual ocean-atmosphere dynamics that occurred during the simulation period that took place from December 2007 to January 2020. We further focused the analysis between 2010 and 2019 to examine the interannual changes in pCO_2 and sea-air CO_2 flux in the region. The analysis period included extreme events, such as the 2015/2016 El Niño and the 2019 positive IOD (pIOD). Previous studies have indicated that unprecedented anomalies occur around the TMC associated with these extreme climate events (e.g., Lu and Ren, 2020; Pujiana et al., 2019) and thus, have become an interesting period to examine the sensitivity of the upper-ocean carbon cycle in the area to such anomalous climate events.

2 Model and datasets

2.1. Model description and configuration

The newly developed ecosystem model employed here was carbon (C) and nutrient (phosphate, nitrate, ammonium) tracing, low-trophic ecosystem model developed by Nakamura et al. (2018). The model was embedded in the Coupled Ocean-Atmosphere-Wave and Sediment Transport (COAWST) modeling environment (Warner et al., 2010) with the Regional Ocean Modeling System (ROMS; Shchepetkin and McWilliams, 2005) as the ocean general circulation model (OGCM). The ecosystem model developed here includes three phytoplankton functional types (PFT) in terms of carbon biomass, comprising diatoms, dinoflagellates, and coccolithophores.

These PFTs utilize nutrients and dissolved inorganic carbon (DIC) for photosynthesis and assimilation. Additionally, coccolithophores further use total alkalinity (TA) for the calcification process to produce $CaCO_3$ shells.

The material excreted by PFTs following the assimilation process immediately enters the labile dissolved organic matter (labile-DOM) pool. All dead phytoplankton biomass enters the particulate organic matter pool as detritus (detritus-POM) and sinks into a deeper layer in the water column. As for the dead coccolithophore biomass, the previously produced $CaCO_3$ from the calcification process enters the particulate inorganic matter ($CaCO_3$-PIM) pool and sinks into a deeper layer, like the detritus-POM. Estimated produced $CaCO_3$-PIM from coccolithophore dead biomass was adapted from Krumhardt et al. (2017, 2019). In this modified version, we have added an inorganic nitrogen compound (nitrate and ammonium) compartment to calculate the effect of nutrient limitation on calcification. Additional sinking velocities for all PFTs in this modified version were applied, following Gregg et al. (2007). One type of zooplankton in terms of carbon biomass was assigned in this model which grazed on phytoplankton, labile-DOM, and detritus-POM. As in the phytoplankton, the dead bodies of zooplankton also entered the detritus-POM pool, with a small part entering the $CaCO_3$-PIM pool. The $CaCO_3$-PIM from zooplankton dead biomass was based on Ishizu et al. (2019, 2020).

The decomposition process takes place in the labile-DOM pool to resupply the inorganic carbon, nitrogen (as ammonium), and phosphorus (as phosphate) needed by phytoplankton. The decomposition of detritus-POM transforms POM into DOM and dissolved inorganic compounds (carbon, nitrogen, and phosphorus) simultaneously. Nitrate in this model was recovered through the nitrification of ammonium. We applied the first order dissolution reaction equation for the dissolution process of $CaCO_3$-PIM with a seawater $CaCO_3$ saturation state that varied within the

water column (Jansen et al., 2002; Sarmiento and Gruber, 2006). Here, the $CaCO_3$-PIM saturation state was approximated as the calcite saturation state, given that the main $CaCO_3$ produced in this model came from coccolithophores.

The pCO_2 was calculated in multiple steps, starting from the estimation of sea surface pH and the concentration of $CO_{2(aq)}$ in the same surface layer. Both pH and $CO_{2(aq)}$ are functions of DIC, TA, water temperature, and salinity, and DIC and TA are generated in the ecosystem module. The sea-air CO_2 flux was calculated based on Wanninkhof (1992), with the CO_2 solubility parameterization adapted from Weiss (1974).

We set the model domain to span from the Southeast Tropical Indian Ocean (SETIO) to the Northwest Pacific Ocean (90° E-164° E; 18° S-29° N). The domain was gridded uniformly with a horizontal resolution of 1/6° × 1/6° while the water column was transformed into 30-layers of non-uniform, terrain-following s-coordinates. Generic length scale (GLS) mixing parameterizations of the k–ε configuration were utilized in this model for vertical mixing combined with the Kantha-Clayson stability function (CPP options KANTHA_CLAYSON) and horizontal smoothing of buoyancy/shear (CPP options N2S2_HORAVG). Smagorinsky-like diffusion (CPP option UV_SMAGORINSKY and TS_SMAGORINSKY) was activated in this simulation for the horizontal diffusion and viscosity for both momentum and tracer variables.

Lateral boundary condition was set to be mixed radiation-nudging for the 3D momentum and tracer variables. The inflow nudging timescale for the temperature/salinity and biogeochemical tracers were set to 100 days and 180 days respectively. In this simulation, some types of material compounds, such as coarse particulate organic matter and refractory dissolved organic matter, were deactivated by setting the value to zero for both the initial and boundary conditions. River

discharge across the model domain was also not implemented; thus, the indicated results of pCO_2 and sea-air CO_2 flux were caused solely by the ocean-atmosphere interaction dynamics.

2.2. Datasets

The Global Ocean Forecasting system (GOFS) analysis/reanalysis product from the hybrid coordinate ocean model (HYCOM; Chassignet et al., 2006) were used as the ocean circulation model initial and boundary conditions in this simulation. Both versions 3.0 and 3.1 of the GOFS output were utilized owing to the difference in the coverage period. We used a three-hourly 55-year Japan reanalysis (JRA-55) product (Kobayashi et al., 2015) as atmospheric forcings in the simulation, which included the atmospheric pressure, air temperature, humidity, wind speed, and cloud fraction. The bulk fluxes (shortwave radiation and longwave radiation) were calculated internally in the model as a function of the sea surface temperature, air temperature, humidity, and cloud fraction. For tidal forcing, Oregon State University Tidal Prediction Software (OTPS) product consisting of 12 tidal components was used.

The initial and boundary conditions for the ecosystem model were generated analytically because of the limitation of seawater carbonate chemistry-related data across the study area. The Global Data Analysis Project (GLODAP) product (Key et al., 2004) which stores scientific cruise data of necessary inorganic carbon parameters such as TA, DIC, and dissolved oxygen (DO), was used and paired with the water temperature data record to create a polynomial equation. This approach allowed us to create a vertically stratified profile for both TA and DIC parameters, which play a crucial role in near-boundary areas. We also estimated the nutrient concentrations for the initial and boundary conditions of the ecosystem model by utilizing the calculated TA, DIC, and salinity data from the GOFS. The equation established here was based on the gradient between the salinity-

normalized DIC (nDIC) and the corresponding nutrient (N, P) from the GLODAP datasets. We found nDIC:P and nDIC:N ratios of 141.23 and 9.76, respectively; hence, this ratio was used for the simulation. The observed nDIC:P and nDIC:N ratios were within the results of previous studies (Martiny et al., 2014; Redfield, 1934; Sarmiento and Gruber, 2006). More details of the analytical equations used to create the initial and boundary conditions of the ecosystem model are provided in Table 1.

Table 1. Analytical equations used to estimate necessary parameters for the ecosystem model simulation in initial and boundary conditions. The equations stated here are functions of water temperature (T), salinity (S), depth (z), and dissolved inorganic carbon (DIC)

Parameter (unit)	**Equation**
Dissolved inorganic carbon (µmol. kg^{-1})	$2312.12 + (10.68 \cdot T) - (3.50 \cdot T^2) + (0.16 \cdot T^3) - (2.42 \times 10^{-3} \cdot T^4)$
Total alkalinity (µmol. kg^{-1})	$2444.73 - (22.29 \cdot T) + (0.09 \cdot T^2) + (1.28 \times 10^{-3} \cdot T^3) + (4.60 \times 10^{-4} \cdot T^4)$
Dissolved oxygen (µmol. L^{-1})	$245.85 - (52.01 \cdot T) + (6.46 \cdot T^2) - (0.28 \cdot T^3) + (3.84 \times 10^{-3} \cdot T^4)$
Phytoplankton (µmolC. L^{-1})	For z < 155 m $\frac{10.5 - 0.00095 \cdot (z + 50)^2}{6}$
Zooplankton (µmolC. L^{-1})	$0.1 \cdot$ Phytoplankton
Nitrate (µmolN. L^{-1})	$0.98 \cdot \frac{\left(\frac{(DIC \cdot 35)}{S} - 1977.4\right)}{9.765}$
Ammonium (µmolN. L^{-1})	$0.02 \cdot \frac{\left(\frac{(DIC \cdot 35)}{S} - 1977.4\right)}{9.765}$

Phosphate (μmolP. L^{-1})	$\frac{\left(\frac{(DIC \cdot 35)}{S} - 1961.3\right)}{141.23}$

185

186 Annual global-averaged atmospheric CO_2 concentration data from 2007 to 2019 recorded by the
187 Earth System Research Laboratory of the National Oceanic and Atmospheric Administration
188 (ESRL NOAA) was used to generate the carbon exchange between the sea surface and atmosphere
189 in the model (https://www.esrl.noaa.gov/gmd/ccgg/trends/global.html). Underway measurement
190 records of seawater CO_2 fugacity (fCO_2) archived in the Surface Ocean CO_2 Atlas (SOCAT)
191 version 2020 (Bakker et al., 2016) were employed for comparison with modeled pCO_2, especially
192 around the Western Pacific Region given its frequent observation. For further simplicity, we
193 regarded both the global-averaged CO_2 concentration and the measured fCO_2 in SOCATv2020 as
194 atmospheric pCO_2 (pCO_{2atm}) and pCO_2 respectively, because of the generally negligible difference
195 between these two parameters and the actual pCO_2 value.

196 Considering the lack of continuous observation data inside the TMC, we only utilized the
197 underway pCO_2 measurements and pCO_2 flux estimation results from several expeditions that
198 were also used by Kartadikaria et al. (2015). The pCO_2 and CO_2 flux data from these expeditions
199 were processed further to remove possible outliers. Outliers were defined as any data below
200 (exceed) the 10^{th} (90^{th}) percentile. Lastly, we calculated both NINO3.4 SSTA and DMI (See Saji
201 et al. 1999 for DMI calculation details) using HadI SST1.1 (Rayner et al. 2003) and the 1961–
202 1990 mean seasonal cycle as the baseline. ENSO events (El Niño/La Niña) were defined whenever
203 the five-month moving average of the NINO3.4 SSTA exceeded the assigned threshold of ± 0.5
204 ^{o}C for at least three consecutive months within the November-March period. A summary of the
205 datasets utilized for this simulation is presented in Table 2.

206 **Table 2.** Summary of datasets utilized for simulation and necessary data analysis

Data Specifications	Sources
Water temperature, salinity, elevation, and velocity (initial and boundary condition of hydrodynamic model)	Global Ocean Forecasting System (GOFS)
Carbonate chemistry and nutrients data (initial and boundary condition of ecosystem model)	Global Data Analysis Project (GLODAP)
Atmospheric forcing	Japanese 55-year reanalysis (JRA-55) product
Tides forcing	Oregon State University Tidal Prediction Software (OTPS)
Annual global-averaged atmosphere's CO_2 concentration	Earth System Research Laboratory of National Oceanic and Atmospheric Administration (ESRL NOAA)
Underway pCO_2 measurements around Western Pacific Ocean	Surface Ocean CO_2 Atlas (SOCAT) version 2020
Underway pCO_2 measurements and sea-air CO_2 flux in Indonesian seas between 2011 and 2013 (used in Kartadikaria et al., 2015)	- Ekspedisi Widya Nusantara (EWIN) - 23 April 2010-5 May 2010 (EWIN 2010) - 13 April 2011-22 April 2011 (EWIN 2011) - 5 June 2013-20 June 2013 (EWIN 2013) - Banggai Expedition - 23 June 2011-7 July 2011 - The South China Sea – Indonesian seas Transport/Exchange (SITE)

	- 22 November 2012-30 November 2012
Climate variability index	NINO3.4 Sea Surface Temperature Anomaly Dipole Mode Index (DMI)

3 Results and discussion

3.1 Comparison with available observations

We separated the SOCAT v2020 data around the Western Pacific Ocean into six longitudinal transect lines from 135° E to 160° E in the following latitudes 0° N, 5° N, 10° N, 15° N, 20° N, 25° N (Figure 1). The monthly value of pCO_2 in each transect line was calculated by averaging all measurement records across the line in the corresponding month. Using this method, we obtained line-averaged monthly pCO_2 data from 2010 to September 2019. For further analysis, we treated the missing value of the area-averaged monthly pCO_2 that did not exceed two consecutive months by using piecewise cubic spline interpolation.

A strong seasonal pattern was exhibited by the Northwestern Pacific Ocean (15° N-25° N) where both model results and observations indicated that high and low pCO_2 occurred in the summer (June-August) and winter (December-February), respectively, which closely follows the seasonal cycle of SST. This implies strong water temperature modulation on pCO_2 in the subtropical Pacific region. However, the seasonal magnitude of pCO_2 weakened around the tropical area from 10° N to 0° N (Figure 1b, lower panel), as the temperature remained relatively stable throughout the year. Long-term linear trend analysis of modeled and observed pCO_2 from 2010 to 2019 showed that the annual increase in pCO_2 also varied with latitude, where the subtropical region experienced faster pCO_2 growth compared with the equatorial area (Table 3). Varying long-term trends across

latitudes were related to atmospheric CO_2 uptake capability, which tends to be stronger in high-latitude areas (Xiu and Chai, 2014).

To examine atmospheric CO_2 sink/source characteristics from observed pCO_2 in the Western Pacific Ocean, we utilized atmospheric pCO_2 (pCO_{2atm}) data from Chuuk Lagoon maintained by the Pacific Marine Environmental Laboratory (PMEL) NOAA Carbon Program (Sutton et al., 2017). The three-hourly recorded pCO_{2atm} from November 2011 to October 2018 was averaged to obtain the monthly average value of pCO_{2atm}. The obtained monthly pCO_{2atm} was then used to calculate the pCO_2 difference between the sea surface and atmosphere ($dpCO_2$), which further dictated the direction of the CO_2 flux at each latitude. A similar procedure was performed for the modeled pCO_2 but using the employed annual global-averaged atmospheric pCO_2 instead. The modeled $dpCO_2$ was in general consistent with the observed $dpCO_2$ with robust correlation ($r = 0.72$; $p < 0.01$) and a bias of 8.70 µatm.

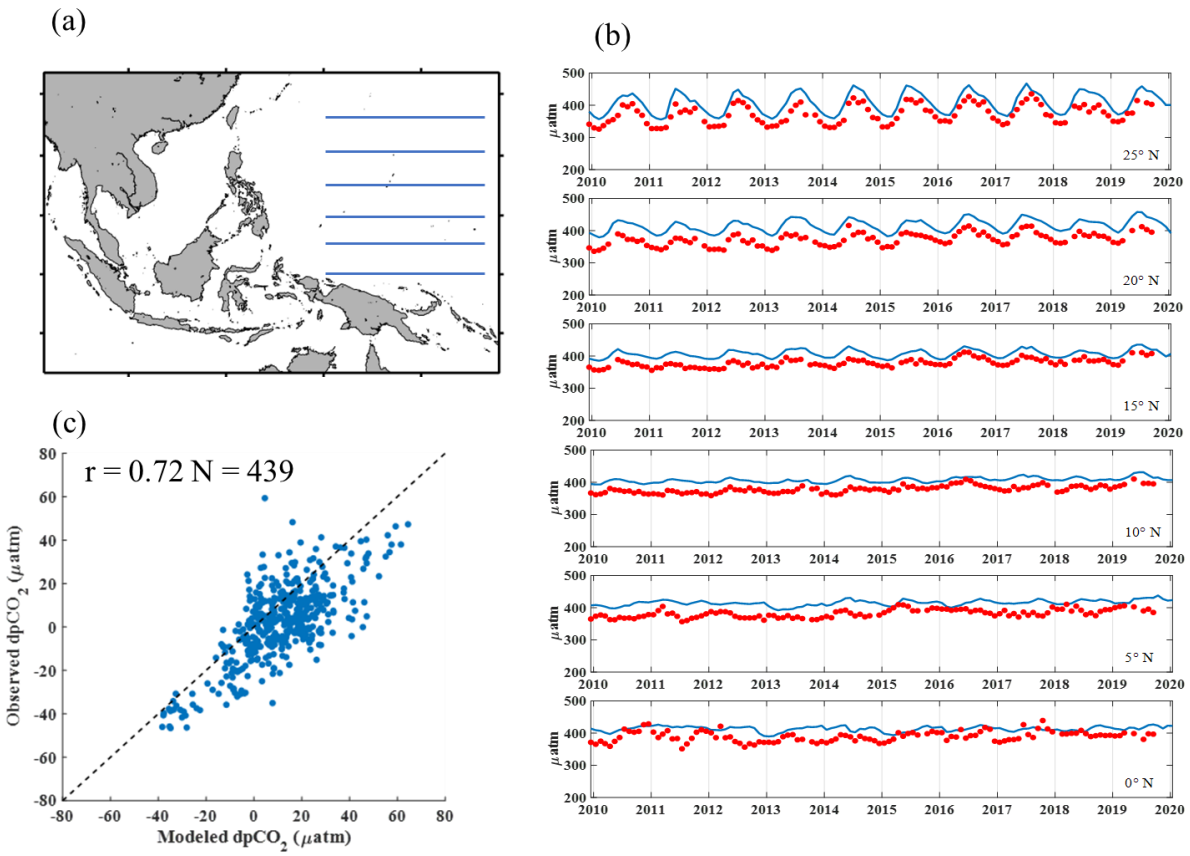

Figure 1. (a) The whole model domain and longitudinal transect lines in the Western Pacific Ocean where SOCATv2020 data was processed and compared with simulation results. (b) Time series of monthly pCO_2 from simulation (blue solid line) and observed (red scatter dots) pCO_2 in the Western Pacific Ocean from equator (0^o N) to 25^o N **l**atitude. (c) Scatter plot between modeled $dpCO_2$ and observed $dpCO_2$. Dashed black line in (c) indicates the 1:1 line where perfect agreement lies.

Table 3. Linear trend analysis results from both observed and modeled pCO_2 across the Western Pacific. Showed trend values were significant at $p < 0.01$.

Annual pCO_2 trend (μatm/year)	25˚ N	20˚ N	15˚ N	10˚ N	5˚ N	0˚ N
SOCAT	3.35	3.51	2.96	2.83	2.69	1.49
Model	2.74	2.47	1.25	1.71	1.26	n/a

The comparison between model results and underway measurements in Indonesian seas also agreed to the extent that the area generally acted as an atmospheric CO_2 source (Table 4). Compared with model results, measured pCO_2 and CO_2 flux by Kartadikaria et al. (2015) showed a higher standard deviation. This emphasizes the urgency of a reliable long-term upper-ocean carbonate chemistry observation system in the area to reduce uncertainty regarding the atmosphere CO_2 sink/source characteristic.

The differences in the modeled pCO_2 with the measured value could be attributed to the spatial variations in biogeochemical dynamics that were not fully resolved by the single-value parameterization approach in the current model configuration. The selection of atmospheric pCO_2 used for the simulation also possibly contributed to this difference. This is based on a comparison between the global-averaged pCO_{2atm}, Chuuk Lagoon monitoring site pCO_{2atm} record (Sutton et al., 2017a), and observed pCO_{2atm} in the study by Kartadikaria et al. (2015), where the global-average pCO_{2atm} was higher than the other measurements.

Table 4. Comparison between observed and modeled pCO_2/CO_2 flux inside the Indonesia Sea between 2010 and 2013 acquired by Kartadikaria et al. (2015). Uncertainty was calculated as one-standard deviation.

Expedition Name	pCO_2 (µatm)		CO_2 flux (gC. m^{-2}. $year^{-1}$)	
	Measured	Modeled	Estimated	Modeled
EWIN 2010	399.43 ± 18.29	436.88 ± 10.19	7.70 ± 5.09	4.23 ± 1.48
EWIN 2011	409.62 ± 10.40	423.79 ± 4.46	6.24 ± 4.82	3.40 ± 0.89
Banggai Expedition 2011	390.21 ± 16.50	415.12 ± 5.82	n/a	8.50 ± 2.94
SITE 2012	416.65 ± 14.20	421.20 ± 7.17	5.77 ± 5.00	1.71 ± 0.66
EWIN 2013	397.46 ± 19.52	439.32 ± 4.00	2.60 ± 5.51	2.70 ± 0.90

3.2. Simulated mean seasonal cycle of the upper-ocean carbon cycle in the Tropical Maritime Continent

Figure 2a shows the simulated pCO_2 with contrasting seasonal cycles between the western and eastern parts of the TMC, consistent with the segregation suggested by Kartadikaria et al. (2015). The western part of the TMC showed a higher pCO_2 than the eastern part during the summer. Conversely, the pattern was reversed during winter, with higher pCO_2 in the eastern part. Large-scale high pCO_2 was observed during spring (March-May), as most of the area across the TMC showed its annual warmest SST, which is a two–three months lag from the peak of winter (Figure 2b). In the succeeding season of the summer-autumn (September-November), an apparent upwelling signature of low SST from along west of Sumatra-south of Java was observed but was associated with high pCO_2 in the area. This further suggests that the effect of SST drop on pCO_2 due to upwelling could be suppressed by the increase in inorganic carbon content, resulting in a net increase in pCO_2.

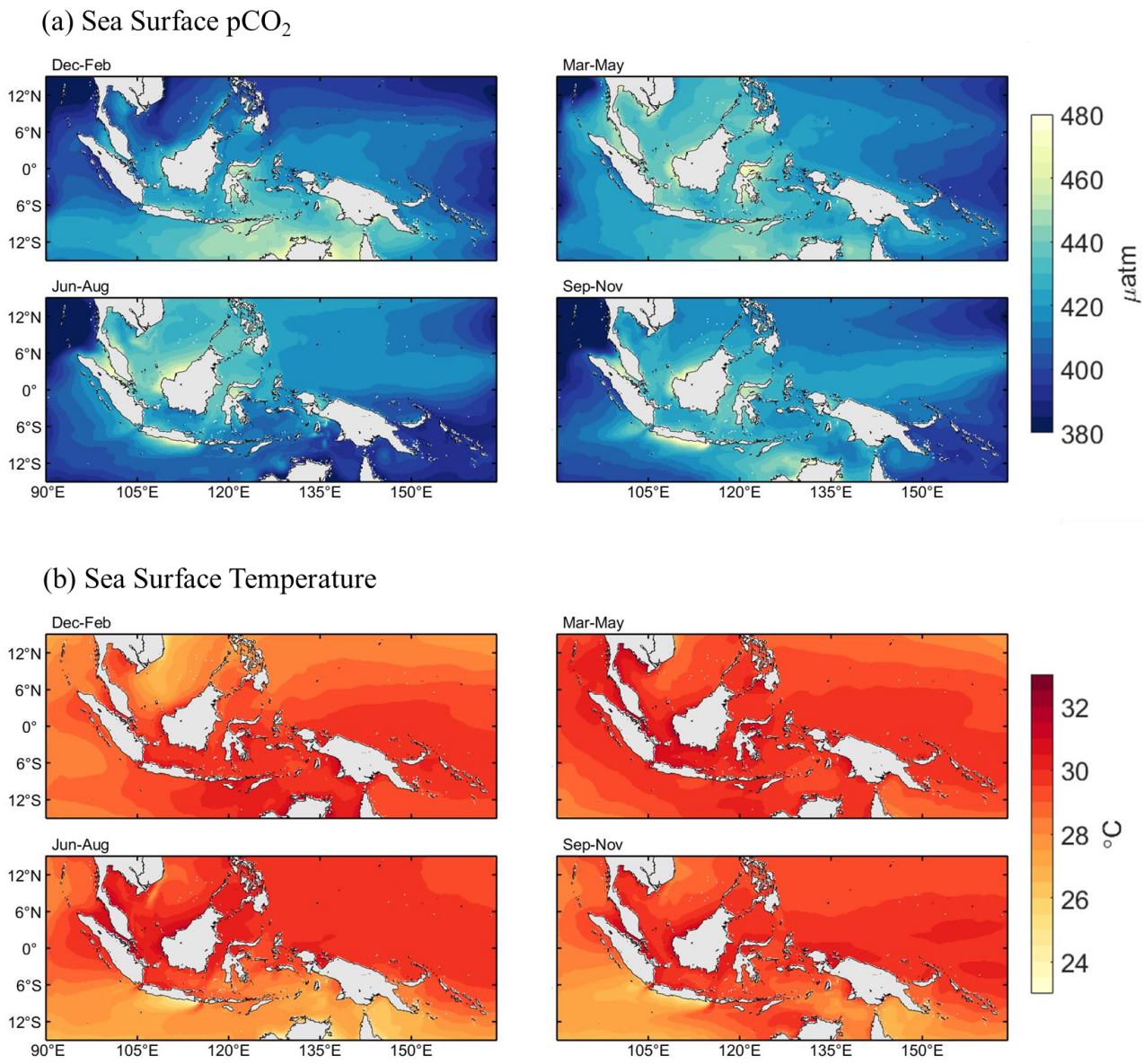

Figure 2. Mean seasonal cycle of modeled (a) sea surface pCO_2 partial pressure (in µatm) and (b) sea surface temperature (in ˚C) over the 2010-2019 period.

The sea-air CO_2 flux seasonal cycle showed that the TMC acted as a full-year atmospheric CO_2 source from sea surface water (Figure 3). Despite the relatively high pCO_2 in spring, the model results suggested weak CO_2 degassing related to the wind speed around the TMC, which was in its

weakest state. Strong CO_2 degassing occurred during the summer, where many areas, such as the southern South China Sea, south of Java, and Southern Makassar Strait, indicate their annual maximum CO_2 flux. In contrast to the other areas, strong CO_2 degassing along the south of Java was further maintained up to the autumn, while in the west of Sumatra, CO_2 degassing peaked at the same time. This made the area the strongest CO_2 source within the TMC according to the simulation results.

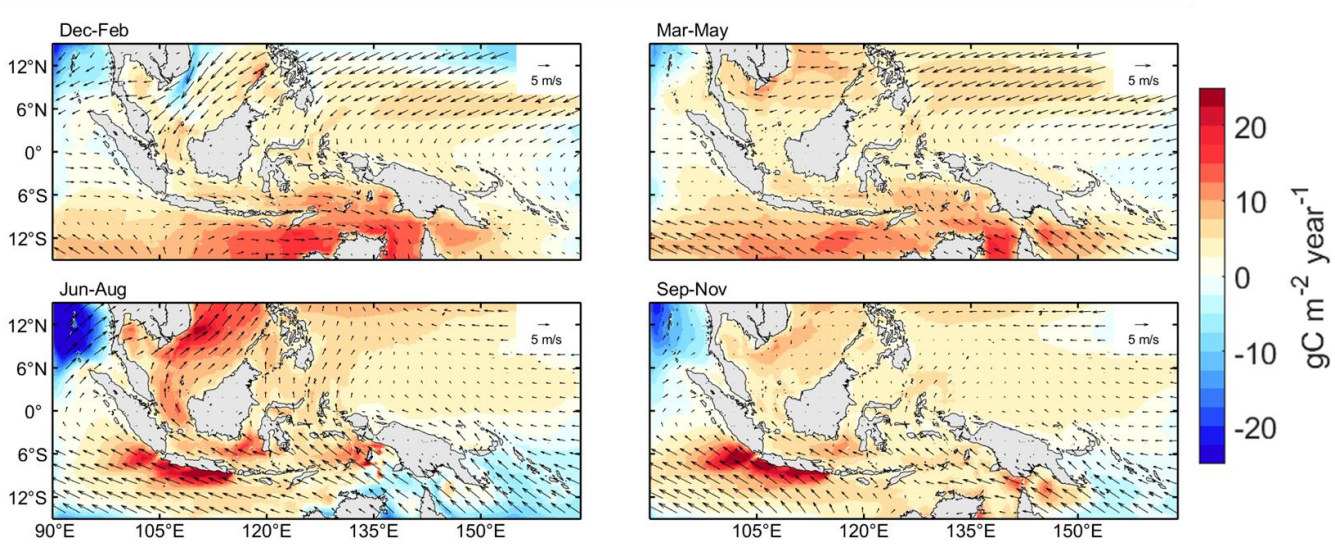

Figure 3. Simulated mean seasonal cycle of sea-air CO_2 flux (**s**haded color; in gC. m^{-2}. $year^{-1}$) across the Tropical Maritime Continent and the corresponding wind speed pattern (vector arrows; in m. s^{-1}) according to the JRA-55 product over the 2010-2019 period. Positive and negative values in the sea-air CO_2 flux indicates atmospheric CO_2 source and sink signature**s**, respectively.

Persisting CO_2 degassing in the south of Java during the summer-autumn could be attributed to the combination of atmospheric forcing and the biogeochemical response of the area to the forcing. Strong wind speeds in the summer created favorable conditions for strong CO_2 degassing in the area through accelerated gas exchange (Figure 4a) and, at the same time, increased the inorganic

303 carbon content in the sea surface during upwelling onset. However, the upwelling itself reached
304 its peak in early autumn, a month after the annual wind stress maxima. This left the area with high
305 inorganic carbon surface water, which further maintained the strong CO_2 degassing condition due
306 to high pCO_2 in the succeeding season.

307 Persisting CO_2 degassing was not apparent through model simulation in the west of Sumatra,
308 despite the similar upwelling seasonality with south of Java (Figure 4b). Instead, our simulation
309 suggested that the peak of CO_2 degassing occurred only in the early autumn, which coincided with
310 peak upwelling. The relatively weaker wind speed compared to south of Java was presumed to be
311 one of the contributing factors to weaker upwelling, both during the onset and peak. The angle of
312 the coast on Sumatra Island and the Coriolis parameter gradient toward latitude, as pointed out by
313 Susanto et al. (2001), further provided additional constraints for the wind to generate coastal
314 upwelling as strong as in the south of Java. We used chlorophyll-a concentration observed by the
315 Moderate Resolution Imaging Spectrometer (MODIS Aqua; Hu et al., 2012) as a proxy for
316 upwelling processes in both west of Sumatra and south of Java. We also calculated the annual
317 average value of Chl:C ratio in the two upwelling areas and found a ratio of 0.02, which was still
318 within the range suggested by Arteaga et al. (2016).

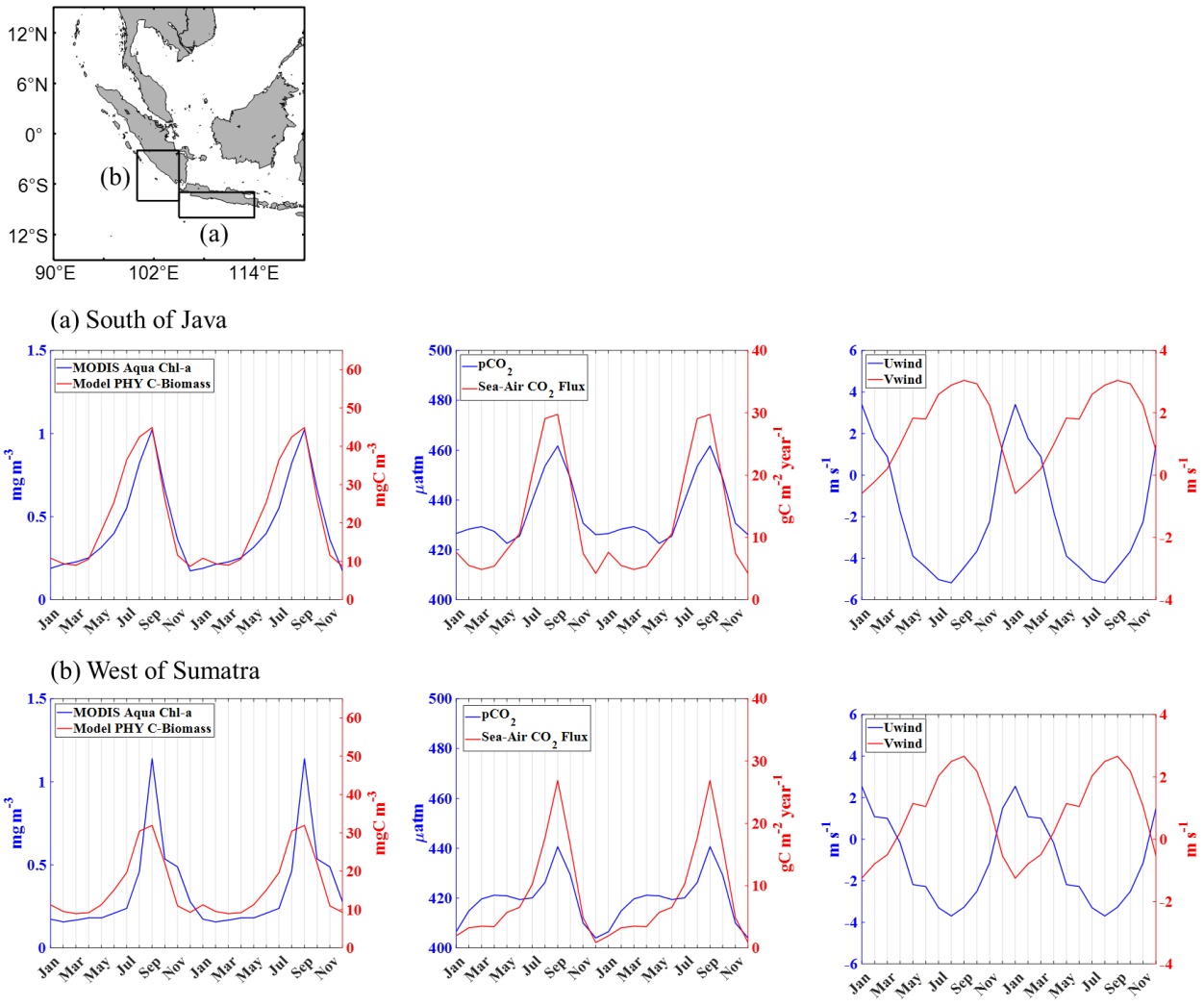

Figure 4. Two full repeated annual cycles of the upwelling system in (a) south of Java and (b) west of Sumatra. Figures include the Chlorophyll-a concentration and simulated phytoplankton carbon biomass (left figures), simulated pCO_2 / sea-air CO_2 flux (middle figures), and wind speed from JRA-55 product (right figures).

3.3 Upper-ocean carbon cycle interannual variability in the Tropical Maritime Continent

The interannual variability was examined by removing the mean seasonal cycle of simulated pCO_2, CO_2 flux, and wind speed from JRA-55 over the 2010–2019 period. As a typical ENSO mature phase occurs within the November-March period, while the IOD occurs in July-November, we

328 focused on the analysis of both pCO_2 and CO_2 flux anomalies in those two periods. Aside from
329 the 2015/2016 El Niño and the 2019 pIOD, there were other ENSO and IOD events reported over
330 the last decade, which can be seen in Table 5.
331
332 **Table 5.** List of Indo-Pacific climatic forcings (ENSO and IOD) over the last decade (2010-2019)
333 according to the NINO3.4 and DMI time series employed in this study

ENSO	IOD
El Niño: 2014/2015, 2015/2016, 2018/2019 La Niña: 2010/2011, 2011/2012, 2017/2018	pIOD: 2011, 2012, 2015, 2017, 2018, 2019 nIOD: 2010, 2013, 2016

334
335 Composited pCO_2 and CO_2 flux anomalies during ENSO years (Figure 5) showed that El Niño
336 was associated with anomalously higher pCO_2 around the TMC. In contrast, La Niña was
337 associated with lower pCO_2. In agreement with the suggestion by Kartadikaria et al. (2015), the
338 anomalous lower pCO_2 during La Niña here corresponded to weaker CO_2 degassing. Our model
339 results further indicated a strong large-scale pCO_2 enhancement during the extreme 2015/2016 El
340 Niño, which corresponded to increased CO_2 degassing within the TMC. The composite analysis
341 provided in Figure 5 also suggested an out-of-phase modulation pattern between the Western
342 Pacific Ocean and TMC during ENSO events over the last decade. This further implied that
343 examination of ENSO influence on the TMC upper-ocean carbon cycle based on the Western
344 Pacific condition should be considered with more caution.

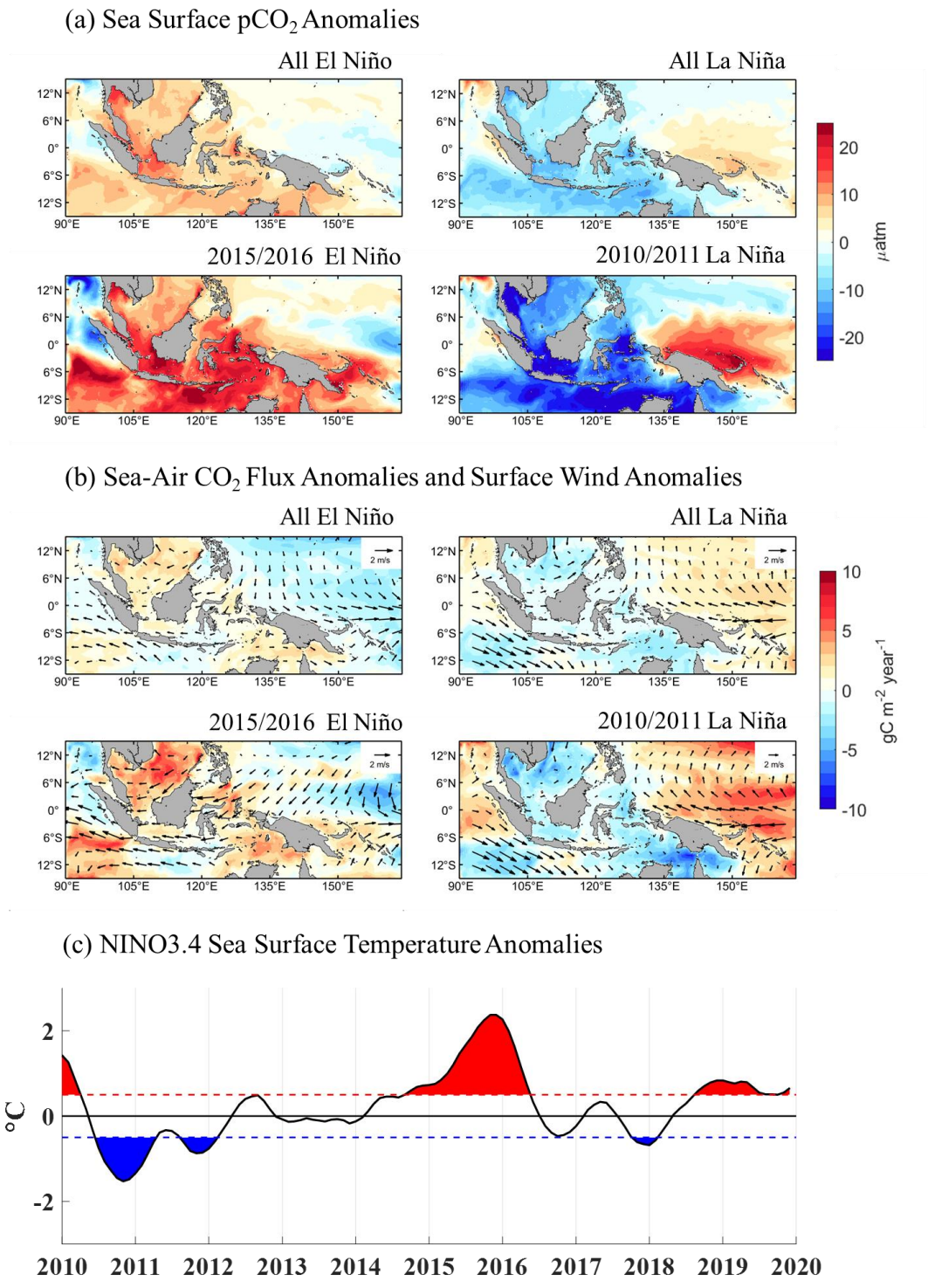

345

346 **Figure 5.** November-March composite average of (a) modeled pCO_2 anomalies (in µatm); (b)

347 modeled sea-air CO_2 flux anomalies (in gC. m^{-2}. $year^{-1}$) with corresponding surface wind

348 anomalies (vector arrows, in m/s) according to the JRA-55 product; and (c) five months moving

349 average of NINO3.4 sea surface temperature anomalies (SSTA). Shaded red and blue color in (c)
350 indicates the period when the SSTA value exceeded/below the +0.5 ^{o}C/-0.5 ^{o}C threshold.
351 Composite average during periods with strong El Niño (2015/2016) and La Niña (2010/2011) were
352 also presented for comparison.
353
354 Apparent anomalous pCO_2 and CO_2 fluxes were observed during IOD event periods, particularly
355 around the west of Sumatra-south of Java (Figure 6). The pIOD was associated with strong pCO_2
356 enhancement and increased CO_2 degassing, whereas under negative IOD (nIOD) conditions, the
357 upper-ocean carbon cycle along the upwelling region showed the opposite modulation pattern.
358 Compared to the composite figures associated with ENSO events, the pCO_2 and CO_2 flux
359 anomalies around West Sumatra-South of Java during IOD events showed more pronounced
360 linearity, where strong anomalies in pCO_2 translated into strong anomalies in CO_2 flux. This could
361 be related to the different pattern of oceanic and atmospheric conditions perturbation caused by
362 these two large-scale climate variabilities, which in IOD cases, are more favorable for stronger
363 CO_2 flux modulation.

364 In addition, to modulation along the west of Sumatra-south of Java, the IOD was also associated
365 with upper-ocean carbon cycle variabilities in the inner part of the TMC, as shown by the
366 composite figure (Figure 6). The model results suggested an anomalous pCO_2 decrease (increase)
367 in the Indonesian seas and northwestern Australia during the pIOD (nIOD). However, a notable
368 decrease (increase) in CO_2 degassing was observed only around northwestern Australia.
369 Contrasting anomaly patterns between the west of Sumatra-south of Java and other areas during
370 IOD events implied different mechanisms controlling the upper-ocean carbon cycle variabilities.
371 Considering the composite analysis provided here, it could be inferred that the 2015-2016 Indo-

372 Pacific climatic forcings (2015 pIOD, 2015/2016 El Niño, and 2016 nIOD) resulted in
373 unprecedented pCO_2 modulation across the TMC over the last decade.

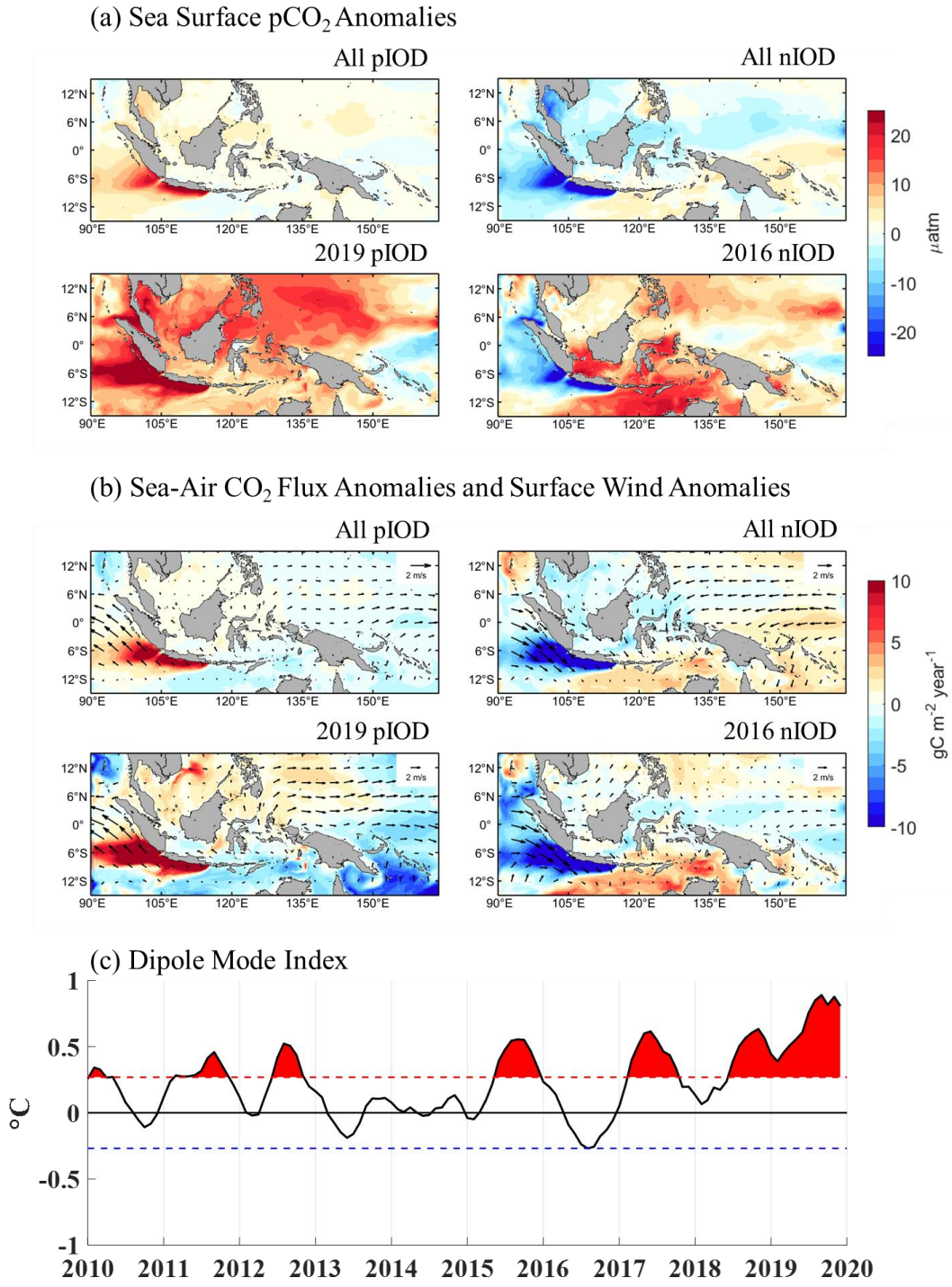

374

Figure 6. July-November composite average of IOD events. (a) Modeled pCO_2 anomalies (in µatm); (b) modeled sea-air CO_2 flux anomalies (in gC. m^{-2}. $year^{-1}$) with corresponding surface wind anomalies (vector arrows, in m/s) according to the JRA-55 product; and (c) five months moving average of NINO3.4 sea surface temperature anomalies (SSTA). Shaded red and blue color in (c) indicates the period when the DMI value exceed/below the one-standard deviation (+1σ/-1σ) threshold. Composite average during the period with strong positive IOD (2019) and negative IOD (2016) were also presented for comparison.

Weaker (stronger) northwest monsoon circulation within the TMC during El Niño (La Niña) due to anomalous divergence (convergence) could weaken (strengthen) the gas exchange between the sea surface and the atmosphere. However, shifts in the Walker circulation caused by the same anomalous divergence (convergence) also altered the cloud distribution across the tropics, including the TMC itself, and affected SST. Decreased (increased) cloud cover around the TMC during El Niño (La Niña) can increase (decrease) SST through an increase (decrease) in incoming solar radiation. This mechanism could increase (decrease) pCO_2 and ultimately strengthen (weaken) CO_2 degassing. The opposite modulation tendencies between atmospheric and oceanic conditions in response to ENSO forcing made the CO_2 flux anomalies magnitude associated with ENSO less pronounced, despite the strong pCO_2 anomalies during the 2015/2016 El Niño or 2010/2011 La Niña.

Conversely, the IOD did not exhibit such opposite tendencies, which resulted in the strong linearity between the pCO_2 anomalies and the CO_2 flux anomalies. Typical IOD events occur between late summer-autumn, where seasonal upwelling occurs (Delman et al., 2016; 2018; Susanto et al., 2001). Anomalous southeasterly (northwesterly) winds during the pIOD (nIOD) around SETIO

can directly modulate upwelling around the west of Sumatra-south of Java. Enhanced (suppressed) upwelling in response to stronger (weaker) wind forcing during pIOD (nIOD) then result in higher (lower)-than-usual pCO_2 from the ocean side and accelerated (decelerated) gas exchange on the atmospheric side.

Furthermore, our model results suggested an asymmetric response of the upper-ocean carbon cycle to IOD over the last decade. The 2016 nIOD, which was not as intense as the preceding 2015 pIOD and far weaker than the 2019 pIOD from the DMI magnitude perspective, showed a comparable modulation in pCO_2 and CO_2 degassing. Scatter plots of pCO_2 anomalies, CO_2 flux anomalies, and phytoplankton carbon biomass concentration anomalies against the DMI showed y-intercept values that fell within the $y < 0$ territory (Figure 7) which depict the asymmetry. Asymmetry response to the IOD was also observed from MODIS observations, implying the robustness of our model in capturing the TMC physical-biogeochemical variabilities associated with the Indo-Pacific climate variabilities.

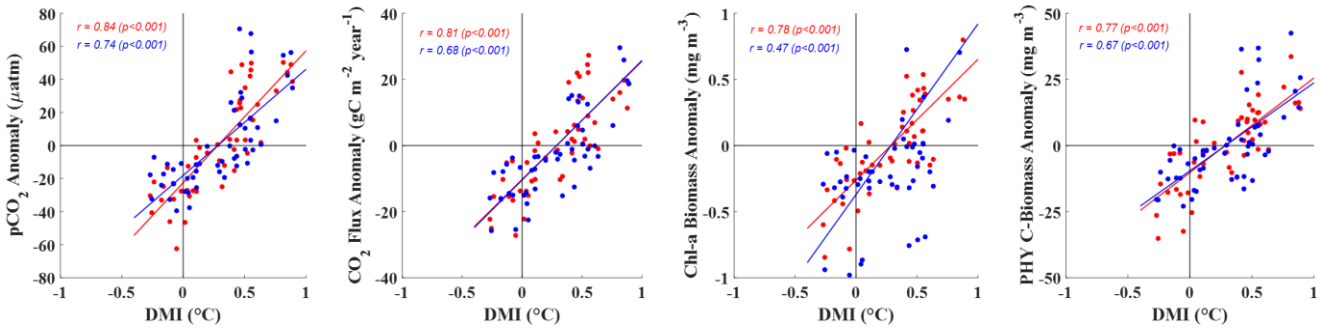

Figure 7. Scatter plot of Chl-a anomaly (in mg. m^{-3}), phytoplankton biomass anomaly (in mgC. m^{-3}), pCO_2 anomaly (in µatm), and CO_2 flux anomaly (in gC. m^{-2}. $year^{-1}$) against DMI around west of Sumatra (blue) and south of Java (red) in July-November over the 2010-2019 period. The red solid line and blue solid line in each scatter graph show the regression model line for south of Java and west of Sumatra, respectively.

The strong asymmetry response to the IOD around the west of Sumatra-south of Java, which was apparent in both simulation results and observations (Chl-a from MODIS Aqua), emphasized the peculiarity of nIOD events over the last decade. Zhang et al. (2018) suggested the contribution of low-frequency thermocline dynamics around the equatorial Indian Ocean to this unusualness, which was most likely captured by the ocean reanalysis product used in this experiment. Anomalous pCO_2 enhancement during nIOD events, especially the 2010 and 2016 nIOD, which extended up to the interior of the Indonesian seas, implied the possibility of another ocean-atmosphere interaction that took place around the TMC. Strong sea surface warming anomalies around the SETIO in the 2010 and 2016 summer, which were also captured by the simulation (not shown), coincided with the demise years of the 2009/2010 and 2015/2016 El Niño. The seasonal timescale difference between the El Niño demise and the appearance of SETIO warming here was in line with Alexander et al. (2002) on the ENSO SST teleconnection pattern, with the Indian Ocean lagging the central Pacific by 3–6 months. A recent review by Cai et al. (2019) further emphasized that such summer warming following El Niño events became prevalent after the 1970s. We presume that while the low-frequency thermocline variabilities may affect upwelling modulation along the west of Sumatra-south of Java during the IOD, the pCO_2 modulation beyond the region during the nIOD was still closely related to the preceding El Niño events.

3.4 Separating the ENSO and IOD influence on the upper-ocean carbon cycle variabilities around the TMC

Since ENSO and IOD showed a statistically significant correlation over 2010-2019 (Pujiana et al., 2019), we further separated the effect of ENSO on IOD and vice versa by performing partial correlation analysis for pCO_2 anomalies, CO_2 flux anomalies, and wind anomalies against DMI and NINO3.4 following the methods of Saji and Yamagata (2003). Regression analysis was conducted to evaluate the extent of each Indo-Pacific climatic forcing in modulating the upper carbon cycle across the TMC over the study period. For uniformity reasoning, we regressed the pCO_2 anomalies, CO_2 flux anomalies, and wind anomalies against the one-standard deviation ($\pm 1\sigma$) of the NINO3.4 ($\sigma_{NINO3.4} = 0.80\ ^oC$) and DMI ($\sigma_{DMI} = 0.26\ ^oC$) over the 2010-2019 period.

Regressed pCO_2 anomalies and CO_2 flux anomalies against one-standard deviation ($\pm 1\sigma$) of NINO3.4 and DMI revealed distinguishable spatial extents of modulation (Figures 8 and 9). Anomalies associated with ENSO during the November-March period tended to have a larger spatial extent, which could reach the SETIO region, compared with IOD during July-November, which was confined along west of Sumatra-south of Java. Results from the regression analysis also showed an extended minor influence of IOD on the carbon cycle variabilities up to the lesser Sunda Island water area and inside the Indonesian seas. Regressed pCO_2 anomalies and CO_2 flux anomalies against the DMI bolster our presumption that IOD alone could not explain notable anomalous pCO_2 enhancement beyond the west of Sumatra-south of Java during recent nIOD events.

Despite regressed pCO_2 anomalies against DMI, which showed a magnitude comparable to the NINO3.4-regressed value, the regressed CO_2 flux anomalies against DMI showed a much higher

458 value. Removing the 2019 pIOD events from the regression analysis (Figure 9, second column)
459 resulted in only slight changes in both pCO_2 anomalies and CO_2 flux anomalies. This implied that
460 even a typical IOD event (after the ENSO influence has been removed) could trigger strong
461 anomalies in the CO_2 flux, especially along the west of Sumatra-south of Java.

462 Regressed pCO_2 anomalies against NINO3.4 further suggested a stronger sensitivity of the TMC
463 to ENSO forcing compared with the adjacent Western Pacific Ocean. The smaller extent of
464 regressed CO_2 flux anomalies against NINO3.4 supported our hypothesis about the apparent
465 nonlinearity between pCO_2 anomalies and CO_2 flux anomalies under the same ENSO events. The
466 exclusion of the 2015/2016 El Niño event in the regression analysis (Figure 8, second column)
467 decreased the magnitude of the pCO_2 anomalies and significantly reduced the spatial extent of the
468 CO_2 flux anomalies. This further suggests that the double-dip La Niña in 2010/2011 and 2011/2012
469 induced less-pronounced CO_2 flux modulation within the TMC. To put into perspective, the 2010–
470 2012 La Niña event occurred for a maximum of 22 months while the 2015–2016 El Niño occurred
471 for 13 months. Both events also showed comparable magnitudes according to the Multivariate
472 ENSO Index v2 (MEIv2; Zhang et al., 2019) in addition to the NINO3.4 SSTA used in this study.
473 It is possible that the Pacific decadal climatic shift in the 2010s modified the ENSO flavor, as
474 pointed out by Newman et al. (2016), including its influence on the TMC, so that CO_2 flux
475 modulation related to the 2015/2016 El Niño showed substantially different characteristics. Further
476 modeling studies across the TMC over a longer time scale will be needed to confirm this possible
477 upper-ocean carbon cycle decadal variation. Note that although removing the extreme events
478 conducted here obviously reduced the standard deviation of NINO3.4 and DMI, the regressed
479 modulation pattern and magnitude against reduced standard deviation did not show significant
480 changes (not shown).

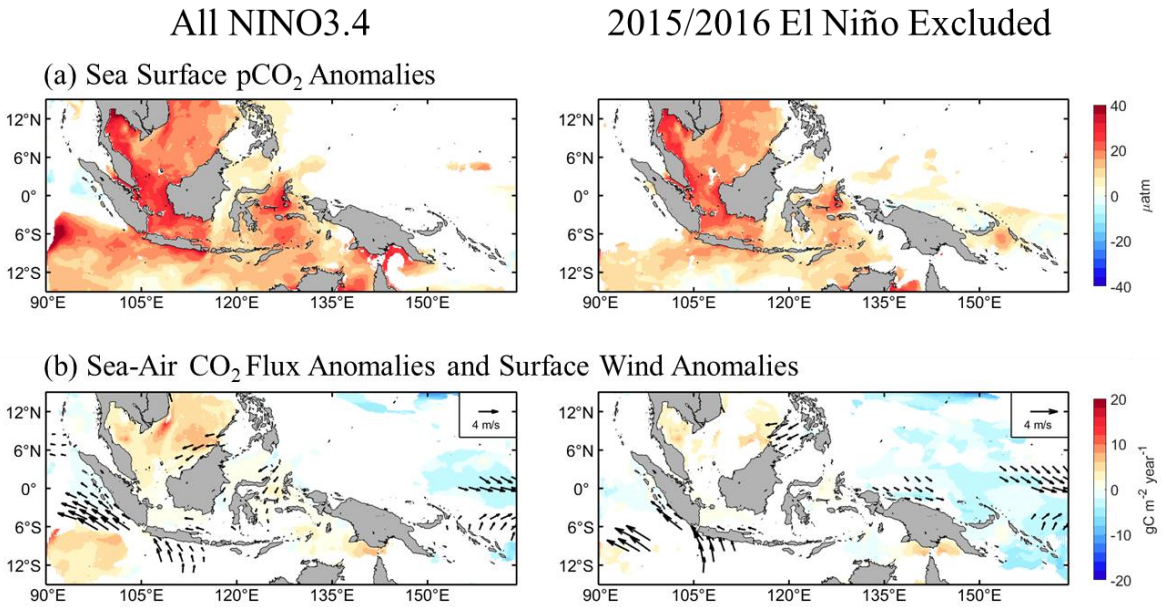

Figure 8. November-March (a) regressed pCO_2 anomalies (in µatm) and (b) regressed CO_2 flux anomalies (in gC. m^{-2}. $year^{-1}$) along with wind anomalies (in m/s) against one-standard deviation of NINO3.4 at zero-lag. Regression was calculated after partialling IOD effect on ENSO. Shaded colors and vector arrows are significant at $p < 0.01$.

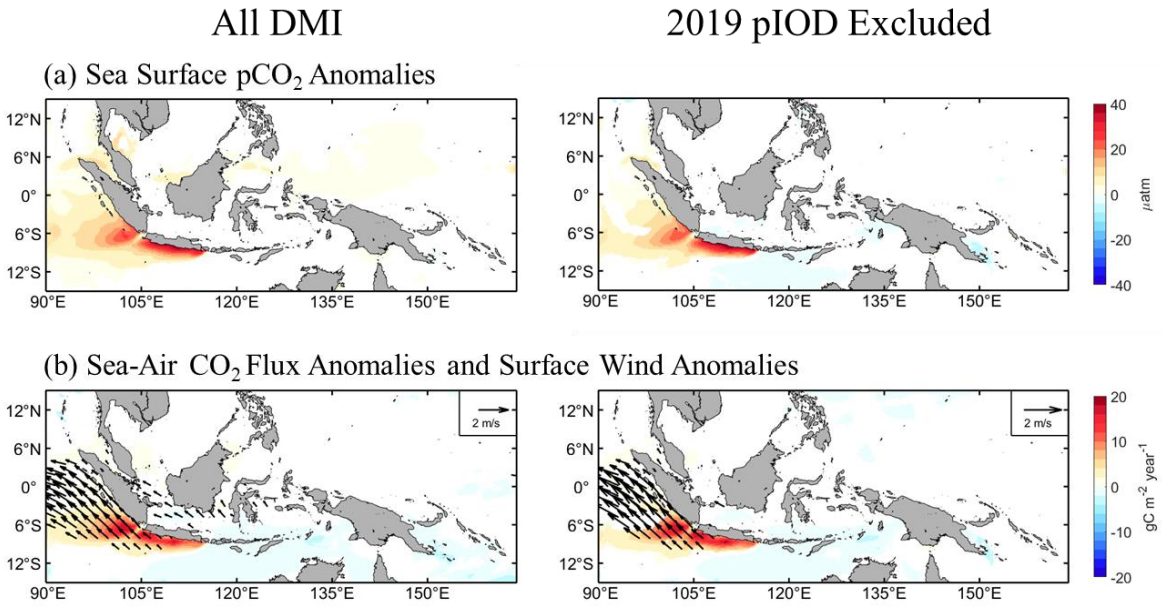

Figure 9. July-November (a) regressed pCO_2 anomalies (in µatm) and (b) regressed CO_2 flux anomalies (in gC. m^{-2}. $year^{-1}$) along with wind anomalies (in m/s) against one-standard deviation of DMI at zero-lag. Regression was calculated after partialling ENSO effect on IOD. Shaded colors and vector arrows are significant at $p < 0.01$.

4 Summary and conclusions

Using a newly developed low-trophic ocean ecosystem model coupled with an OGCM, we examined the upper-ocean carbon cycle variabilities over the last decade in the TMC, where long-term observations in the area remained limited. By utilizing a suite of realistic atmospheric and oceanic analysis/reanalysis products, we aimed to generate ocean dynamics under a series of climate variabilities between 2010 and 2019 as realistic as possible to reduce the uncertainty caused by overlooked ocean-atmosphere interactions. We also proposed a treatment for the initial and boundary conditions in the ecosystem model that allowed us to approximate the vertical structure of the important ecosystem parameters in the model.

In general, the model could capture the basic seasonality of the carbon cycle exhibited by available observations along with its spatial variations, albeit some differences, especially in pCO_2, which might be related to the selection of atmospheric CO_2 forcing used in this simulation and some not-yet-involved biogeochemical processes (e.g., silicate dynamics and iron dynamics). Nevertheless, produced atmospheric CO_2 sink/source characteristic from this modeling study were in agreement with previous studies (Bakker et al., 2016; Chai et al., 2009; Hamzah et al., 2020; Kartadikaria et al., 2015; Sutton et al., 2017; Xiu and Chai, 2014). This enabled us to further analyze the produced upper-ocean carbon cycle variabilities in response to the forcing used in the simulation experiment.

While acted as full-year atmospheric CO_2 source with area-averaged flux equivalent to 0.08 PgC per year, our simulation results indicated pronounced seasonality along the west of Sumatra-south of Java. Strong seasonal winds that triggered upwelling around the area (Horii et al., 2018; Ningsih et al., 2013: Siswanto et al., 2020; Susanto et al., 2001) created favorable conditions for strong CO_2 degassing through a combination of accelerated gas exchange and an abundant supply of subsurface inorganic carbon. This mechanism was not apparent in other areas across the TMC, making it an unique feature of the upper-ocean carbon cycle perspective. Note that the aggregate results of upwelling to carbon cycling might vary across regions (Chakraborty et al., 2018; Valsala et al., 2014) and thus, the results presented by this model for the west of Sumatra-south of Java should not be taken as a generalization for all upwelling-active regions.

Composite analysis of both pCO_2 anomalies and CO_2 flux anomalies clearly showed pronounced features that could be related to Indo-Pacific climate variability (ENSO and IOD) over the last decade. Strong anomalous pCO_2 enhancement along with stronger-than-usual CO_2 degassing occurred from 2015 and lasted until (at least) the 2016 summer, making it the largest and longest upper ocean carbon cycle modulation in the TMC according to the simulation results. The sequence of IOD and ENSO events between 2015-2016 (2015 pIOD and 2015/2016 El Niño) was strongly related to this unprecedented modulation over the last decade. The modulations were then swung toward the negative territory (i.e., decreased pCO_2 and reduced CO_2 degassing) as the 2016 nIOD gained momentum. We further suggested the distinctive modulation characteristic associated with ENSO and IOD, which caused the magnitude of the CO_2 flux variability during ENSO to be lower than that during IOD.

An attempt to elucidate the extent of extreme climate events (2015/2016 El Niño and 2019 pIOD) influence on the upper-ocean carbon cycle across the TMC through regression analysis yielded

notable results. It can be inferred that recent extreme climate events were likely responsible for a larger extent of upper-ocean carbon modulation around the TMC over the last decade. Considering the simulation results and analysis conducted here, further pronounced modulation of the upper-ocean carbon cycle across the TMC can be expected, as recent studies have indicated an intensification of extreme climate anomalies under the effect of greenhouse gas forcing (Cai et al., 2018; Grothe et al., 2019; Zhang et al., 2018).

Finally, one of the biggest challenges hindering this study was that we could not incorporate river discharge in the simulation experiment. The lack of reliable datasets, especially for carbonate chemistry-related parameters, such as DIC, TA, and nutrients, as highlighted by Valsala et al. (2014), was the main reason for this limitation. Such data are critical for evaluating the robustness of any regional-scale watershed modeling effort before further use in coupled OGCM-ecosystem models. Incorporating river discharge inappropriately for studying upper-ocean carbon cycle variability will only produce questionable results. DIC from river discharge, for example, varies widely between river mouths, with values ranging from 284 μmol. kg^{-1} (Rosentreter and Eyre, 2019) to as high as 3,500 μmol. kg^{-1} (Kawahata et al., 2000). This highly variable value did not include the possible strong seasonal and interannual variability of the river-discharged material, as presumed by Xiu and Chai (2014). Regardless of the limitations of this study, the results presented here could invite interdisciplinary research collaborations to establish a continuous oceanic carbon cycle monitoring system across the TMC and enrich our understanding of its dynamics under changing environments.

Acknowledgments

This study was funded by Science and Technology Research Partnership for Sustainable Development through the "Comprehensive Assessment and Conservation of Blue Carbon Ecosystem and their Services in the Coral Triangle (*Blue*CARES)" Project. The first author is a scholarship recipient from Japan's ministry of education, culture, sports, science, and technology (MEXT). We are grateful for the high-performance computing services 'TSUBAME 3.0' provided by the Tokyo Institute of Technology for making this simulation experiment possible.

Data Availability Statement

The original code of our model and necessary code to prepare the input for simulation experiment can be accessed at https://github.com/NakamuraTakashi. Further guidance on how to utilize the codes can be requested through personal communication with Faisal Amri (amri.f.aa@m.titech.ac.jp/faisal.amri.os12@gmail.com) or Takashi Nakamura (nakamura.t.av@m.titech.ac.jp). The Surface Ocean CO_2 Atlas (SOCAT) datasets can be accessed through https://www.socat.info. Global sea surface temperature from HadISST1.1 used for calculating the NINO3.4 and DMI can be retrieved from https://www.metoffice.gov.uk/hadobs/hadisst/. Information about pCO_2 observation and sea-air CO_2 flux estimation data in Indonesia sea used in this study can be requested through personal communication with A.R. Kartadikaria (aditya.kartadikaria@kaust.edu.sa) or Atsushi Watanabe (a-watanabe@spf.or.jp).

References

Alexander, M. A., Bladé, I., Newman, M., Lanzante, J. R., Lau, N. C., & Scott, J. D. (2002). The atmospheric bridge: The influence of ENSO teleconnections on air-sea interaction over the global oceans. Journal of Climate, 15(16), 2205–2231. https://doi.org/10.1175/1520-0442(2002)015<2205:TABTIO>2.0.CO;2

Arteaga, L., Pahlow, M., & Oschlies, A. (2016). Modeled Chl:C ratio and derived estimates of phytoplankton carbon biomass and its contribution to total particulate organic carbon in the global surface ocean. Global Biogeochemical Cycles, 30(12), 1791–1810. https://doi.org/10.1002/2016GB005458

Ashok, K., Guan, Z., & Yamagata, T. (2003). A look at the relationship between the ENSO and the Indian Ocean Dipole. Journal of the Meteorological Society of Japan. https://doi.org/10.2151/jmsj.81.41

Ashok, K., Behera, S. K., Rao, S. A., Weng, H., & Yamagata, T. (2007). El Niño Modoki and its possible teleconnection. Journal of Geophysical Research: Oceans. https://doi.org/10.1029/2006JC003798

Bakker, D. C. E., Pfeil, B., Landa, C. S., Metzl, N., O'Brien, K. M., Olsen, A., Smith, K., Cosca, C., Harasawa, S., Jones, S. D., Nakaoka, S. I., Nojiri, Y., Schuster, U., Steinhoff, T., Sweeney, C., Takahashi, T., Tilbrook, B., Wada, C., Wanninkhof, R., … Xu, S. (2016). A multi-decade record of high-quality fCO2 data in version 3 of the Surface Ocean CO2 Atlas (SOCAT). In Earth System Science Data. https://doi.org/10.5194/essd-8-383-2016

595 Banzon, V., Smith, T. M., Steele, M., Huang, B., & Zhang, H. M. (2020). Improved estimation of
596 proxy sea surface temperature in the arctic. Journal of Atmospheric and Oceanic
597 Technology, 37(2), 341–349. https://doi.org/10.1175/JTECH-D-19-0177.1

598 Cai, W., Wang, G., Gan, B., Wu, L., Santoso, A., Lin, X., et al.. (2018). Stabilised frequency of
599 extreme positive Indian Ocean Dipole under 1.5°C warming. Nature Communications,
600 9(1), 4–11. https://doi.org/10.1038/s41467-018-03789-6

601 Cai, W., Wu, L., Lengaigne, M., Li, T., McGregor, S., Kug, J. S., et al. (2019). Pantropical climate
602 interactions. Science, 363(6430). https://doi.org/10.1126/science.aav4236

603 Chai, F., Liu, G., Xue, H., Shi, L., Chao, Y., Tseng, C. M., et al.. (2009). Seasonal and interannual
604 variability of carbon cycle in South China Sea: A three-dimensional physical-
605 biogeochemical modeling study. Journal of Oceanography.
606 https://doi.org/10.1007/s10872-009-0061-5

607 Chakraborty, K., Valsala, V., Gupta, G. V. M., & Sarma, V. V. S. S. (2018). Dominant Biological
608 Control Over Upwelling on pCO2 in Sea East of Sri Lanka. Journal of Geophysical
609 Research: Biogeosciences, 123(10), 3250–3261. https://doi.org/10.1029/2018JG004446

610 Chassignet, E. P., Hurlburt, H. E., Smedstad, O. M., Halliwell, G. R., Hogan, P. J., Wallcraft, A.
611 J., & Bleck, R. (2006). Ocean prediction with the Hybrid Coordinate Ocean Model
612 (HYCOM). In Ocean Weather Forecasting: An Integrated View of Oceanography.
613 https://doi.org/10.1007/1-4020-4028-8_16

614 Delman, A. S., Sprintall, J., McClean, J. L., & Talley, L. D. (2016). Anomalous Java cooling at
615 the initiation of positive Indian Ocean Dipole events. Journal of Geophysical Research:
616 Oceans. https://doi.org/10.1002/2016JC011635

617 Delman, A. S., McClean, J. L., Sprintall, J., Talley, L. D., & Bryan, F. O. (2018). Process-Specific
618 Contributions to Anomalous Java Mixed Layer Cooling During Positive IOD Events.
619 Journal of Geophysical Research: Oceans, 123(6), 4153–4176.
620 https://doi.org/10.1029/2017JC013749

621 Gordon, A. L. (1986). Interocean exchange of thermocline water. Journal of Geophysical
622 Research. https://doi.org/10.1029/jc091ic04p05037

623 Gregg, W. W., & Casey, N. W. (2007). Modeling coccolithophores in the global oceans. Deep-
624 Sea Research Part II: Topical Studies in Oceanography.
625 https://doi.org/10.1016/j.dsr2.2006.12.007

626 Grothe, P. R., Cobb, K. M., Liguori, G., Di Lorenzo, E., Capotondi, A., Lu, Y., et al.. (2020).
627 Enhanced El Niño–Southern Oscillation Variability in Recent Decades. Geophysical
628 Research Letters, 47(7), 1–8. https://doi.org/10.1029/2019GL083906

629 Hamzah, F., Agustiadi, T., Susanto, R. D., Wei, Z., Guo, L., Cao, Z., & Dai, M. (2020). Dynamics
630 of the Carbonate System in the Western Indonesian Seas During the Southeast Monsoon.
631 Journal of Geophysical Research: Oceans. https://doi.org/10.1029/2018JC014912

632 Horii, T., Ueki, I., & Ando, K. (2018). Coastal upwelling events along the southern coast of Java
633 during the 2008 positive Indian Ocean Dipole. Journal of Oceanography, 74(5), 499–508.
634 https://doi.org/10.1007/s10872-018-0475-z

635 Hu, C., Lee, Z., & Franz, B. (2012). Chlorophyll a algorithms for oligotrophic oceans: A novel
636 approach based on three-band reflectance difference. Journal of Geophysical Research:
637 Oceans. https://doi.org/10.1029/2011JC007395

638 Iida, Y., Kojima, A., Takatani, Y., Nakano, T., Sugimoto, H., Midorikawa, T., & Ishii, M. (2015).
639 Trends in pCO2 and sea–air CO2 flux over the global open oceans for the last two decades.
640 Journal of Oceanography. https://doi.org/10.1007/s10872-015-0306-4

641 Ishizu, M., Miyazawa, Y., Tsunoda, T., & Guo, X. (2019). Development of a biogeochemical and
642 carbon model related to ocean acidification indices with an operational ocean model
643 product in the North Western Pacific. Sustainability (Switzerland), 11(9).
644 https://doi.org/10.3390/su11092677

645 Ishizu, M., Miyazawa, Y., Tsunoda, T., & Guo, X. (2020). Seasonal variability in the inorganic
646 ocean carbon cycle in the Northwest Pacific evaluated using a biogeochemical and carbon
647 model coupled with an operational ocean model. Climatic Change.
648 https://doi.org/10.1007/s10584-020-02779-2

649 Jansen, H., Zeebe, R. E., & Wolf-Gladrow, D. A. (2002). Modeling the dissolution of settling
650 CaCO3 in the ocean. Global Biogeochemical Cycles, 16(2), 11-1-11–16.
651 https://doi.org/10.1029/2000gb001279

652 Kartadikaria, A. R., Watanabe, A., Nadaoka, K., Adi, N. S., Prayitno, H. B., Soemorumekso, S.,
653 Muchtar, M., Triyulianti, I., Setiawan, A., Suratno, S., & Khasanah, E. N. (2015). CO_2
654 sink/source characteristics in the tropical Indonesian seas. Journal of Geophysical
655 Research: Oceans. https://doi.org/10.1002/2015JC010925

656 Kawahata, H., Yukino, I., & Suzuki, A. (2000). Terrestrial influences on the Shiraho fringing reef,
657 Ishigaki Island, Japan: High carbon input relative to phosphate. Coral Reefs, 19(2), 172–
658 178. https://doi.org/10.1007/s003380000093

659 Key, R. M., Kozyr, A., Sabine, C. L., Lee, K., Wanninkhof, R., Bullister, J. L., et al.. (2004). A
660 global ocean carbon climatology: Results from Global Data Analysis Project (GLODAP).
661 Global Biogeochemical Cycles, 18(4), 1–23. https://doi.org/10.1029/2004GB002247

662 Kobayashi, S., Ota, Y., Harada, Y., Ebita, A., Moriya, M., Onoda, H., et al.. (2015). The JRA-55
663 reanalysis: General specifications and basic characteristics. Journal of the Meteorological
664 Society of Japan, 93(1), 5–48. https://doi.org/10.2151/jmsj.2015-001

665 Krumhardt, K. M., Lovenduski, N. S., Iglesias-Rodriguez, M. D., & Kleypas, J. A. (2017).
666 Coccolithophore growth and calcification in a changing ocean. Progress in Oceanography,
667 159(June), 276–295. https://doi.org/10.1016/j.pocean.2017.10.007

668 Krumhardt, K. M., Lovenduski, N. S., Long, M. C., Levy, M., Lindsay, K., Moore, J. K., & Nissen,
669 C. (2019). Coccolithophore Growth and Calcification in an Acidified Ocean: Insights From
670 Community Earth System Model Simulations. Journal of Advances in Modeling Earth
671 Systems, 11(5), 1418–1437. https://doi.org/10.1029/2018MS001483

672 Li, Y., Chen, Q., Liu, X., Li, J., Xing, N., Xie, F., et al. (2019). Long-Term Trend of the Tropical
673 Pacific Trade Winds Under Global Warming and Its Causes. Journal of Geophysical
674 Research: Oceans, 124(4), 2626–2640. https://doi.org/10.1029/2018JC014603

675 Lu, B., & Ren, H. L. (2020). What Caused the Extreme Indian Ocean Dipole Event in 2019?
676 Geophysical Research Letters. https://doi.org/10.1029/2020GL087768

677 Martiny, A. C., Vrugt, J. A., & Lomas, M. W. (2014). Concentrations and ratios of particulate
678 organic carbon, nitrogen, and phosphorus in the global ocean. Scientific Data, 1, 1–7.
679 https://doi.org/10.1038/sdata.2014.48

680 Nakamura, T., Nadaoka, K., Watanabe, A., Yamamoto, T., Miyajima, T., & Blanco, A. C. (2018).
681 Reef-scale modeling of coral calcification responses to ocean acidification and sea-level
682 rise. Coral Reefs, 37(1), 37–53. https://doi.org/10.1007/s00338-017-1632-3

683 Newman, M., Alexander, M. A., Ault, T. R., Cobb, K. M., Deser, C., Di Lorenzo, E., et al. (2016).
684 The Pacific decadal oscillation, revisited. Journal of Climate, 29(12), 4399–4427.
685 https://doi.org/10.1175/JCLI-D-15-0508.1

686 Ningsih, N. S., Rakhmaputeri, N., & Harto, A. B. (2013). Upwelling variability along the southern
687 coast of Bali and in Nusa Tenggara waters. Ocean Science Journal, 48(1), 49–57.
688 https://doi.org/10.1007/s12601-013-0004-3

689 Obata, A., & Kitamura, Y. (2003). Interannual variability of the sea-air exchange of CO2 from
690 1961 to 1998 simulated with a global ocean circulation-biogeochemistry model. Journal of
691 Geophysical Research: Oceans. https://doi.org/10.1029/2001jc001088

692 Pujiana, K., McPhaden, M. J., Gordon, A. L., & Napitu, A. M. (2019). Unprecedented Response
693 of Indonesian Throughflow to Anomalous Indo-Pacific Climatic Forcing in 2016. Journal
694 of Geophysical Research: Oceans, 124(6), 3737–3754.
695 https://doi.org/10.1029/2018JC014574

696 Pujiana, K., & McPhaden, M. J. (2020). Intraseasonal Kelvin Waves in the Equatorial Indian
697 Ocean and Their Propagation into the Indonesian Seas. Journal of Geophysical Research:
698 Oceans. https://doi.org/10.1029/2019JC015839

699 Rayner, N. A., Parker, D. E., Horton, E. B., Folland, C. K., Alexander, L. V., Rowell, D. P., et al.
700 (2003). Global analyses of sea surface temperature, sea ice, and night marine air

temperature since the late nineteenth century. Journal of Geophysical Research: Atmospheres, 108(14). https://doi.org/10.1029/2002jd002670

Redfield, A.C. (1934). On The Proportion of Organic Derivatives in Sea Water and Their Relation to The Composition of Plankton. James Johnstone Memorial Volume, 176-192

Rosentreter, J. A., & Eyre, B. D. (2020). Alkalinity and dissolved inorganic carbon exports from tropical and subtropical river catchments discharging to the Great Barrier Reef, Australia. Hydrological Processes, 34(7), 1530–1544. https://doi.org/10.1002/hyp.13679

Saji, N. H., Goswami, P. N., Vinayachandran, P. N., & Yamagata, T. (1999). A dipole mode in the tropical indain ocean. Nature, 401(September), 360–363. https://doi.org/10.1038/43854

Saji, N. H., & Yamagata, T. (2003). Possible impacts of Indian Ocean Dipole mode events on global climate. Climate Research. https://doi.org/10.3354/cr025151

Sarmiento, J.L., Gruber, N. (2006). Ocean Biogeochemical Dynamics. Princeton U. Press. ISBN 978-0-691-01707-5

Shchepetkin, A. F., & McWilliams, J. C. (2005). The regional oceanic modeling system (ROMS): A split-explicit, free-surface, topography-following-coordinate oceanic model. Ocean Modelling, 9(4), 347–404. https://doi.org/10.1016/j.ocemod.2004.08.002

Siswanto, E., Horii, T., Iskandar, I., Gaol, J. L., Setiawan, R. Y., & Susanto, R. D. (2020). Impacts of climate changes on the phytoplankton biomass of the Indonesian Maritime Continent. Journal of Marine Systems. https://doi.org/10.1016/j.jmarsys.2020.103451

Susanto, R. D., Gordon, A. L., & Zheng, Q. (2001). Upwelling along the coasts of Java and Sumatra and its relation to ENSO. Geophysical Research Letters. https://doi.org/10.1029/2000GL011844

723 Sutton, Adrienne J.; Sabine, Christopher L.; Noh, Jae-Hoon; Lee, Charity M.; Musielewicz,
724 Sylvia; Maenner Jones, Stacy; Dietrich, Colin; Bott, Randy; Osborne, John (2017a). High-
725 resolution ocean and atmosphere pCO2 time-series measurements from mooring
726 ChuukK1_152E_7N in the North Pacific Ocean (NCEI Accession 0157443). Subset used:
727 December 2014 - October 2018. NOAA National Centers for Environmental Information.
728 Dataset. https://doi.org/10.3334/cdiac/otg.tsm_chuukk1_152e_7n . Accessed 12/10/2020.

729 Sutton, A. J., Wanninkhof, R., Sabine, C. L., Feely, R. A., Cronin, M. F., & Weller, R. A. (2017b).
730 Variability and trends in surface seawater pCO2 and CO2 flux in the Pacific Ocean.
731 Geophysical Research Letters, 44(11), 5627–5636.
732 https://doi.org/10.1002/2017GL073814

733 Sprintall, J., Gordon, A. L., Koch-Larrouy, A., Lee, T., Potemra, J. T., Pujiana, K., & Wijffels, S.
734 E. (2014). The Indonesian seas and their role in the coupled ocean-climate system. Nature
735 Geoscience. https://doi.org/10.1038/ngeo2188

736 Syamsudin, F., Kaneko, A., & Haidvogel, D. B. (2004). Numerical and observational estimates of
737 Indian Ocean Kelvin wave intrusion into Lombok Strait. Geophysical Research Letters.
738 https://doi.org/10.1029/2004GL021227

739 Takahashi, T., Sutherland, S. C., Sweeney, C., Poisson, A., Metzl, N., Tilbrook, B., et al.. (2002).
740 Global sea-air CO2 flux based on climatological surface ocean pCO2, and seasonal
741 biological and temperature effects. Deep-Sea Research Part II: Topical Studies in
742 Oceanography. https://doi.org/10.1016/S0967-0645(02)00003-6

743 Takahashi, T., Sutherland, S. C., Wanninkhof, R., Sweeney, C., Feely, R. A., Chipman, D. W., et
744 al.. (2009). Climatological mean and decadal change in surface ocean pCO2, and net sea-

745 air CO2 flux over the global oceans. Deep-Sea Research Part II: Topical Studies in
746 Oceanography. https://doi.org/10.1016/j.dsr2.2008.12.009

747 Valsala, V. K., Roxy, M. K., Ashok, K., & Murtugudde, R. (2014). Spatiotemporal characteristics
748 of seasonal to multidecadal variability of pCO2 and air-sea CO2 fluxes in the equatorial
749 Pacific Ocean. Journal of Geophysical Research : Oceans.
750 https://doi.org/10.1002/2014JC010212

751 Wanninkhof, R. (1992). Relationship between wind speed and gas exchange over the ocean.
752 Journal of Geophysical Research, 97(C5), 7373–7382. https://doi.org/10.1029/92JC00188

753 Weiss, R.F. (1974). Carbon Dioxide in Water and Seawtaer: The Solubility of A Non-Ideal Gas.
754 Marine Chemistry, 2(1974), 203-2015. https://doi.org/10.1016/0304-4203(74)90015-2

755 Warner, J. C., Armstrong, B., He, R., & Zambon, J. B. (2010). Development of a Coupled Ocean-
756 Atmosphere-Wave-Sediment Transport (COAWST) Modeling System. Ocean Modelling,
757 35(3), 230–244. https://doi.org/10.1016/j.ocemod.2010.07.010

758 Wyrtki, K. (1961). Physical Oceanography of the Southeast Asian Waters. Naga Report Volume
759 2. Scientific Results of Marine Investigation of the South China Sea and the Gulf of
760 Thailand 1959-1961.

761 Xiu, P., & Chai, F. (2014). Variability of oceanic carbon cycle in the North Pacific from seasonal
762 to decadal scales. Journal of Geophysical Research: Oceans, 119(8), 5270–5288.
763 https://doi.org/10.1002/2013jc009505

764 Zhang, L., Du, Y., & Cai, W. (2018). Low-Frequency Variability and the Unusual Indian Ocean
765 Dipole Events in 2015 and 2016. Geophysical Research Letters, 45(2), 1040–1048.
766 https://doi.org/10.1002/2017GL076003

767 Zhang, T., Hoell, A., Perlwitz, J., Eischeid, J., Murray, D., Hoerling, M., & Hamill, T. M. (2019).
768 Towards Probabilistic Multivariate ENSO Monitoring. Geophysical Research Letters,
769 46(17–18), 10532–10540. https://doi.org/10.1029/2019GL083946